Hindawi
Advances in Civil Engineering
Volume 2024, Article ID 5375733, 12 pages
https://doi.org/10.1155/2024/5375733

Research Article

Goaf Site Stability Detection in the Overlap Area of Coal Mining Subsidence and Urban Construction

Guangli Dai ,[1] Hongjia Li ,[2] Chao Liu ,[1] Huaizhan Li ,[2] Youwei Chang ,[1] Yu Chen ,[2] Yandong Gao ,[2] Yafei Yuan ,[2] and Wenqi Huo [2]

[1]*Fifth Geological Brigade, Geology and Mineral Resources Bureau of Jiangsu, Xuzhou 221116, China*
[2]*School of Environment and Spatial Informatics, China University of Mining and Technology, Xuzhou 221116, China*

Correspondence should be addressed to Hongjia Li; ts22160126p31@cumt.edu.cn

Received 26 July 2023; Revised 7 March 2024; Accepted 13 March 2024; Published 27 March 2024

Academic Editor: Bruno Briseghella

The contradiction between coal mining and urban construction in coal resource-based cities is prominent, which greatly limits the sustainable development of these cities. Pan'an New City is a key mining-induced subsidence area in Xuzhou City, which presents significant challenges to the construction of the new city. Therefore, in order to ensure the safe construction of Pan'an New City, the residual deformation and stability of the goaf sites must be monitored and evaluated. Under such background, based on the measured leveling data of the mining-induced surface deformation in a coal mine near Pan'an New City, this paper first analyzed the accuracy of InSAR monitoring of surface deformation in coal mining subsidence area by SBAS-InSAR technology. Then, the SBAS-InSAR technology was used to monitor the surface subsidence rate and cumulative subsidence in the coal mining subsidence area of Pan'an New City, based on the 29 scene SAR data during Dec. 2020 and Jan. 2022. The results showed that the goaf site in the north and northwest of Pan'an New City is unstable, while the other areas are stable. Finally, according to the monitoring results, the suggestions have been put forward for the construction of Pan'an New Town on the goaf site. The research results have important theoretical and practical significance for the reuse of goaf sites in Pan'an New City and similar areas in Xuzhou.

1. Introduction

Xuzhou is a prefecture-level city in Jiangsu Province, China, with a total area of 11,765 km^2 and a recorded population of 9,028,500. It has become a national innovation demonstration area for sustainable development and won the UN-Habitat Scroll of Honor Award in 2018. With the population growth and urban development of Xuzhou, the industrial lands and residential lands are expanding to the surrounding areas, of which Pan'an New Town is an important node of Xuzhou's expansion to the east. However, the Pan'an Lake area was once the largest and most serious coal mining subsidence area in Xuzhou City, with the accumulated area of coal mining subsidence of 11.6 km^2, and the deepest subsidence of 18 m as well as severe ponding [1]. After more than a decade of rehabilitation and ecological transformation, the waterlogged area has been renovated into a national 4A-level wetland park [2]. The coal mining subsidence lands without waterlogging have carried out land reclamation and ecological restoration. Such transformations are favorable for construction and development of the Pan'an New City.

After underground coal mining, the goaf and the fractured rock mass above it are in a relatively equilibrium state after a long period of natural compaction. However, cracks, separation layers, and cavities in the overburden of the goaf will break the equilibrium state under the action of various internal and external loads, such as building loads, vibration loads, seismic forces, and groundwater. Thus, the secondary surface subsidence will be formed, which is called the activation of the old goaf [3]. The poor foundation site formed by coal mining collapse in the Pan'an Lake area has posed a serious restriction and potential safety hazard to the construction of Pan'an New City. Therefore, it is necessary to monitor the deformation and stability of mining subsidence in the planning area of Pan'an New City.

The commonly used surface deformation monitoring methods include geodetic surveying [4, 5], GNSS monitoring method [6], 3D laser scanning method [7], UAV monitoring [8], InSAR technology [9–11], etc. The planning scheme of Pan'an New City in Jiawang District has been initiated since 2020/08/28, and the follow-up monitoring of coal mining subsidence sites was conducted by InSAR technology with the advantages of all-weather, low-cost, and large-scale monitoring [12–14]. However, D-InSAR technology also presents many defects in the application of surface deformation monitoring. D-InSAR technology surgery is easily affected by various discoherence factors, mainly time weak correlation and space weak correlation as well as multiple error phase interference is often involved in the process of obtaining interference phase information [15, 16]. In order to solve the problems faced by the above traditional D-InSAR technology, multi-temporal InSAR (MT-InSAR), which used multiview SAR images simultaneously, were further developed on this basis. Among them, persistent scatterer InSAR (PS-InSAR) technique is the most typical. This method first analyzes the scattering characteristics of each pixel in the time dimension of the sequential SAR image and selects the target of high coherence point which is less affected by noise and spatiotemporal weak correlation [17]. Persistent scatterer (PS) analysis is used to improve the accuracy and reliability of surface subsidence monitoring, but in order to ensure the reliability of PS points, but it has strict requirements on the number of images.

In order to avoid the above problem, small baseline subset (SBAS) technology was proposed. This method mainly takes advantage of the feature that the interference pair of short space-time baseline may be less affected by space-time desiccating and obtains the interference pair set of free combination through the space-time baseline threshold [18]. A large number of coherent targets (CTs) are screened by coherence coefficient and other threshold values to improve the reliability of monitoring results. Under ideal conditions, the deformation monitoring accuracy of the above methods can reach millimeter or even submillimeter level theoretically [19]. Compared with other measurement methods, it does not need to establish a monitoring network and has the function of trace analysis, which is very suitable for deformation monitoring in this area [20–22]. Baek et al. [23] obtained 23 JERS-1L-band SAR data covering Gangwon mining area in South Korea and monitored the temporal subsidence of the mining area by SBAS [23]. Cianflone et al. [24] used the small temporal baseline subset (STBAS) to Envisat and COSMO SkyMed satellites to study the temporal and spatial characteristics of surface subsidence in Sibari Plain in Southern Italy [24]. Han et al. [25] obtained the images of ALOS-1, Envisat, and Sentinel-1 from 2007 to 2010, 2008 and 2010, and 2015 to 2019, respectively, through multitemporal InSAR technology and investigated and revealed the spatial–temporal evolution of surface subsidence in Wuhan. In general, the time-series InSAR monitoring technology can be used to monitor the deformation of surface subsidence in Pan'an New City. What is more, there has been a blank in SBAS-InSAR monitoring of residual deformation and site stability detection of mining subsidence area, based on which we give some advice to construct this area.

In order to assess the stability of mining-induced surface subsidence and provide technical support for the planning of the design of Pan'an New City, the measured data of mining-induced surface deformation from coal mines near Xuzhou will be used to verify and analyze the accuracy of SBAS-InSAR in monitoring the surface deformation. Then, the surface subsidence, deformation, and stability of Pan'an New City will be monitored by InSAR technology. The research results are of important practical significance for the safety construction of Pan'an New City.

2. Materials and Methods

In order to ensure the reliability of the surface deformation results of Pan'an New City by SBAS-InSAR technique, a working face in a coal mine, 140 km away from Pan'an New City was taken as the research object. The accuracy of surface deformation of Pan'an New City and its surrounding areas by SBAS-InSAR was verified by comparing the measured data of the surface deformation of the working face and the SBAS-InSAR monitoring results.

2.1. Overview of the Study Area. The study area is 8,311 and 8,312 working faces in 830 mining area of a mine in Shandong province, about 140 km away from Pan'an New City, as shown in Figure 1. Under the jurisdiction of Rencheng District, Jining City, Shandong Province, it is 7.2 km long from north to south, 9 km wide from east to west, and covers an area of about 65 km^2. The mining activities began in June 2019. The surface movement observation stations were set and fourth-class leveling was adopted for regular monitoring. The average mining depth was about 400 m, and the average mining thickness was about 2.2 m. The 8,311 working face advanced 429 m and the 8,312 working face advanced 164 m. The fully mechanized mining with paste filling technology was used for mining.

2.2. Data Preparation and Processing. The data source was from the Sentinel-1A satellite data, and SBAS-InSAR technology was used. Sentinel-1A IW SAR images were used, which are characterized with relatively low azimuth resolution and a wider range of imaging made up of multiple stripes. Twenty-eight images were obtained between 2020/07/15 and 2021/06/04, as shown in Table 1. The azimuth and range resolutions were 13.9 and 2.3 m, respectively.

Meanwhile, the all-region SRTM 90 m resolution DEM data were downloaded from the official website (https://www.usgs.gov/) of the U.S. Geological Survey (USGS) to assist interferogram coregistration and remove the terrain phase information from the interferometric phase. The precise satellite orbit data corresponding to SAR images were obtained from the official website of Sentinel-1A satellite precise orbit data to reduce the orbit errors in the interferometric phase and improve the coregistration accuracy.

2.2.1. Technical Principle of SBAS-InSAR Technology. The research point is called slowly decorrelating filtered phase (SDFP) point in SBAS-InSAR technology [26]. The candidate points were selected through amplitude dispersion index DA whose threshold value was 0.6. SDFP pixels were identified among candidate pixels in the same way as selecting PS points. The spatially correlated phases of interferometric phase were estimated by bandpass filtering surrounding pixels. The spatially

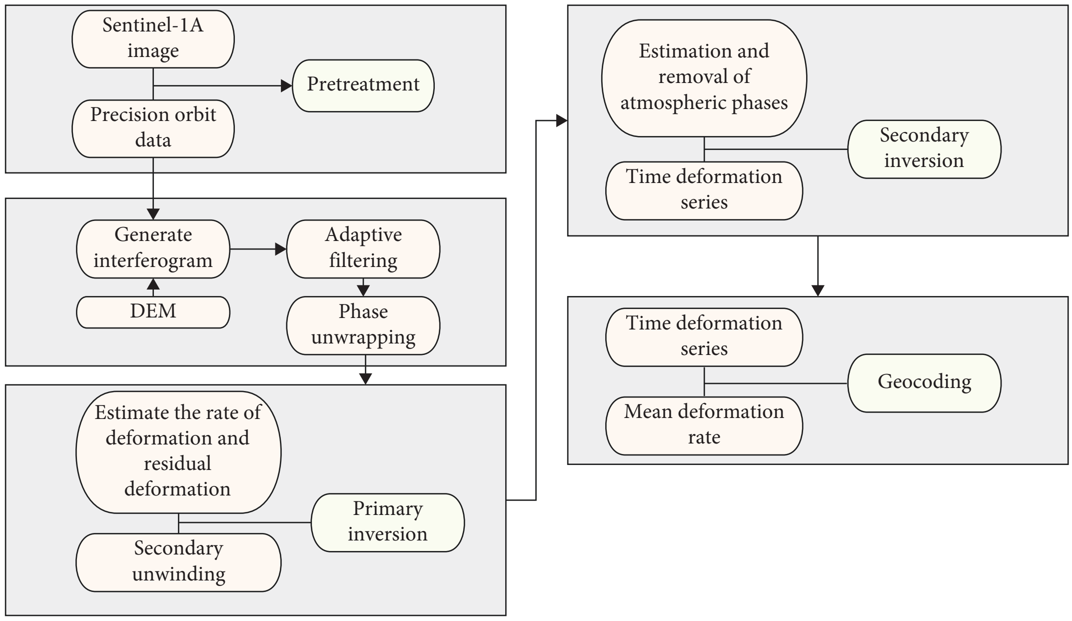

Figure 1: Data processing.

Table 1: Sentinel-1A image data information.

No.	Satellite	Date	Orbit	No.	Satellite	Date	Orbit
1	Sentinel-1	2020/07/15	Ascending	15	Sentinel-1	2020/12/30	Ascending
2	Sentinel-1	2020/07/27	Ascending	16	Sentinel-1	2021/01/11	Ascending
3	Sentinel-1	2020/08/08	Ascending	17	Sentinel-1	2021/01/23	Ascending
4	Sentinel-1	2020/08/20	Ascending	18	Sentinel-1	2021/02/04	Ascending
5	Sentinel-1	2020/09/01	Ascending	19	Sentinel-1	2021/02/16	Ascending
6	Sentinel-1	2020/09/13	Ascending	20	Sentinel-1	2021/02/28	Ascending
7	Sentinel-1	2020/09/25	Ascending	21	Sentinel-1	2021/03/12	Ascending
8	Sentinel-1	2020/10/07	Ascending	22	Sentinel-1	2021/03/24	Ascending
9	Sentinel-1	2020/10/19	Ascending	23	Sentinel-1	2021/04/05	Ascending
10	Sentinel-1	2020/10/31	Ascending	24	Sentinel-1	2021/04/17	Ascending
11	Sentinel-1	2020/11/12	Ascending	25	Sentinel-1	2021/04/29	Ascending
12	Sentinel-1	2020/11/24	Ascending	26	Sentinel-1	2021/05/11	Ascending
13	Sentinel-1	2020/12/06	Ascending	27	Sentinel-1	2021/05/23	Ascending
14	Sentinel-1	2020/12/18	Ascending	28	Sentinel-1	2021/06/04	Ascending

uncorrelated parallax errors were estimated by correlation with the vertical baseline, including elevation errors and deviations of pixel phase center from its physical center. The two estimate values were subtracted to get an estimate of pixel-correlated noise which was characterized by coherence:

$$\gamma_x = \frac{1}{N}\left|\sum_{i=1}^{N}\exp\left\{\sqrt{-1}\left(\psi_{x,i} - \tilde{\psi}_{x,i} - \Delta\widehat{\phi}^{u}_{\text{topo},x,i}\right)\right\}\right|, \tag{1}$$

where $\psi_{x,i}$ represents the winding phase of the ith interferogram of pixel x, $\tilde{\psi}_{x,i}$ represents the spatially correlated estimate, $\Delta\widehat{\phi}^{u}{}_{\text{topo},x,i}$ represents the spatially uncorrelated line-of-sight error estimate, and N refers to the number of interferograms.

The same algorithm was used to select PS and SDFP pixels, but the final results were different due to the application of different interference pair sets. After the two estimates were removed from the original wrapped phase, a 3D phase unwrapping algorithm was applied for unwrapping and the results are as follows:

$$\widehat{\phi}_{x,i} = \phi_{D,x,i} + \phi_{A,x,i} + \Delta\phi_{S,x,i} + \Delta\phi^{c}_{\theta,x,i} + \Delta\phi_{N,x,i} + 2k_{x,i}\pi, \tag{2}$$

where $\widehat{\phi}_{x,i}$ is the unwrapped phase and $k_{x,i}$ is the remaining unknown whole week ambiguity. If the unwrapping result was accurate enough, $k_{x,i}$ would be the same integer for most pixels x in the given interferogram i.

After the unwrapping result was obtained, there were still some phases unavailable to get deformed phase $\phi_{D,x,i}$. The spatial correlation phases except the deformation phase were divided into the temporal correlation phases and the unexpected phases, including the contributions of the primary image $\phi_{A,x,i} + \Delta\phi_{S,x,i}$ and the secondary images $\phi_{A,x,i} + \Delta\phi_{S,x,i}$ and $\Delta\phi^{c}_{\theta,x,i}$. They were estimated separately by using a combination of temporal and spatial filtering. A low-pass filter in the time domain was used to estimate the spatial correlation phases. Under the influence of $k_{x,i}$, $\widehat{\phi}_{x,i}$ was irrelevant in the time domain and could not be filtered directly in the time domain. However, for most adjacent SDFP pixels, $k_{x,i}$ was the same, so the calculation of phase difference between adjacent SDFP pixels could basically eliminate the item of $2k_{x,i}\pi$ and filter the result phase. First, Delaunay triangulation was used to form a spatial network connecting all SDFP pixels. In each interferogram, the equation of $\widehat{\phi}_{x,i}$, between SDFP pixel pairs around each triangle in the clockwise direction, is given as follows:

$$\Delta^{x_2}_{x_1}\widehat{\phi}_{x,i} = \Delta^{x_2}_{x_1}\phi_{D,x,i} + \Delta^{x_2}_{x_1}\phi_{A,x,i} + \Delta^{x_2}_{x_1}\Delta\phi_{S,x,i} + \Delta^{x_2}_{x_1}\Delta\phi^{c}_{\theta,x,i} + \Delta^{x_2}_{x_1}\Delta\phi_{N,x,i} + \Delta^{x_2}_{x_1}2k_{x,i}\pi, \tag{3}$$

where $\Delta^{x_2}_{x_1}$ refers to the difference between x_2 and x_1. For each pair of coherent points, the differential phase could be low-pass filtered by using the Gaussian function to generate convolution:

$$L^{T}\left\{\Delta^{x_2}_{x_1}\widehat{\phi}_{x,i}\right\} \approx \Delta^{x_2}_{x_1}\phi_{D,i} - \Delta^{x_2}_{x_1}\phi^{m}_{A} - \Delta^{x_2}_{x_1}\Delta\phi^{m}_{S}, \tag{4}$$

where LT $\{\cdot\}$ refers to the low-pass filtering operation, and the superscript m refers to the contribution of the primary images to these items.

In order to maintain the deformation phase, the Gaussian filter width was less than the expected change time of the deformation rate. With the estimate of the acquisition time of the primary images $L^{T}\{\Delta^{x_2}_{x_1}\widehat{\phi}_{x,i}\}$, the deformation phase of all pixels was zero, so the estimate of $\Delta^{x_2}_{x_1}\phi^{m}_{A} + \Delta^{x_2}_{x_1}\Delta\phi^{m}_{S}$ could be obtained. The $\phi^{m}_{A} - \Delta\phi^{m}_{S}$ of arbitrary reference pixel could be obtained by least square method.

In order to estimate the contribution of the spatially correlated phase of the secondary image that was irrelevant of expected time, the time-domain high pass filter was applied to the phase difference between adjacent SDFP pixels. The following equation could be obtained by using Equation (3) – Equation (4):

$$\Delta^{x_2}_{x_1}\widehat{\phi}_{x,i} - L^{T}\left\{\Delta^{x_2}_{x_1}\widehat{\phi}_{x,i}\right\} \approx \Delta^{x_2}_{x_1}\phi^{S}_{A,i} + \Delta^{x_2}_{x_1}\Delta\phi^{S}_{S,i} + \Delta^{x_2}_{x_1}\Delta\phi^{c}_{\theta,i} + \Delta^{x_2}_{x_1}\Delta\phi_{N,i}. \tag{5}$$

The superscript s refers to the contributions of the secondary image. For each interferogram, the high pass filtered signal of each SDFP pixel relative to any reference SDFP pixel could be calculated by equation by the least square method:

$$\left[\Delta^{x_2}_{x_1}\right]^{-1}\left\{\Delta^{x_2}_{x_1}\widehat{\phi}_{x,i} - L^{T}\left\{\Delta^{x_2}_{x_1}\widehat{\phi}_{x,i}\right\}\right\} \approx \phi^{S}_{A,x,i} + \Delta\phi^{S}_{S,x,i} + \Delta\phi^{c}_{\theta,x,i} + \Delta\phi_{N,x,i}. \tag{6}$$

Then, the spatial phase of each interferogram was low-pass filtered by convolving the 2D Gaussian function. The width of the Gaussian convolution was generally set to be very narrow, usually 50 m, to include all signals except those localized to a single SDFP pixel. The following equation can be obtained:

$$\phi_{D,x,i} - \Delta\phi_{N,x,i} - 2k_{x,i}\pi \approx \widehat{\phi}_{x,i} + \left(\widehat{\phi}^{m}_{A,x} + \Delta\widehat{\phi}^{m}_{S,x}\right) - \left(\phi^{S}_{A,x,i} + \Delta\phi^{S}_{S,x,i} + \Delta\phi^{c}_{\theta,x,i}\right). \tag{7}$$

The obtained unwrapping phase was believed to eliminate the influence of $2k_{x,i}\pi$ in the whole interferogram, and the final results only included the deformation phase, spatial uncorrelated noise, and unwrapping errors. Figure 1 shows the specific data processing.

In radar imaging, microwave signals sent by antennas pass through the atmosphere and interact with the earth's surface before being reflected back and recorded by sensors. However, some of the effects that exist in InSAR observations cannot fully eliminated by filters. The application of InSAR in surface deformation detection is mainly restricted by two factors, time weak correlation and atmospheric influence. The former relates to the interaction between radar waves and the surface. As to Pan'an New City, the correlation is always higher in urban areas. The latter relates to the interaction between radar waves and the atmosphere including ionospheric [27], tropospheric [28–31], etc. Even though there are ways to make them weaker, it is hard to eliminate them.

2.2.2. Monitoring Accuracy Analysis. In order to evaluate the accuracy of SBAS-InSAR monitoring the surface deformation of coal mining in Pan'an New City and surrounding areas, the leveling data of 40 observation stations above the 8,311 and 8,312 working faces were used for verification. The leveling time was from 2020/07/18 to 2021/05/26. Figure 2 shows the location relationship between the benchmark and the working faces.

The methodology of converting LOS angle to vertical is quite complete [32, 33]. In order to further explain the influence of horizontal movement on the accuracy of InSAR monitoring, and mitigate the errors caused by the position mismatch between level observation station and high coherence point, image resolution, etc., leveling was used to monitor the accuracy [20].

During the measuring time, the accumulated subsidence monitored by InSAR was processed and compared with the

Figure 2: Distribution of observation points.

Table 2: Comparison between observation data and InSAR data.

No.	Bench mark (mm)	InSAR (mm)	Error (mm)
L1	−1	−5.19	4.19
L3	0	−6.91	6.91
L8	−3	−9.94	6.94
L10	−5	−10.21	5.21
L11	−5	−11.84	6.84
L12	−6	−12.03	6.03
L13	−11	−12.30	1.3
L14	−8	−13.21	5.21
L15	−10	−15.02	5.02
L16	−14	−16.82	2.82
n1	−36	−40.41	4.41
n3	−36	−33.56	2.44
n4	−27	−30.11	3.11
n6	−31	−33.42	2.42
n8	−43	−37.21	5.79
n9	−32	−37.33	5.33

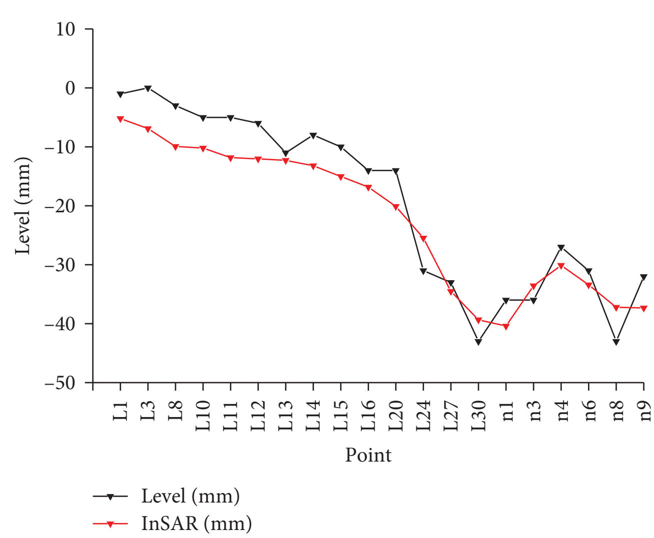

Figure 3: Comparison between InSAR monitoring results and measured data in the study area.

measured data of 40 observation benchmarks, as shown in Table 2. Figure 3 shows the comparison of InSAR monitoring results and measured data in the study area.

Meanwhile, the cumulative settlement of the same observation point and the corresponding SBAS-InSAR monitoring data were extracted as two variables. Their deviation degree and correlation were statistically analyzed by using R-squared and RMSE, as shown in Figure 4. The mean x of the cumulative settlement is −17.525 mm, and the average value y of InSAR processing result is −21.823 mm. The correlation coefficient R of the two groups of data is 0.9805,

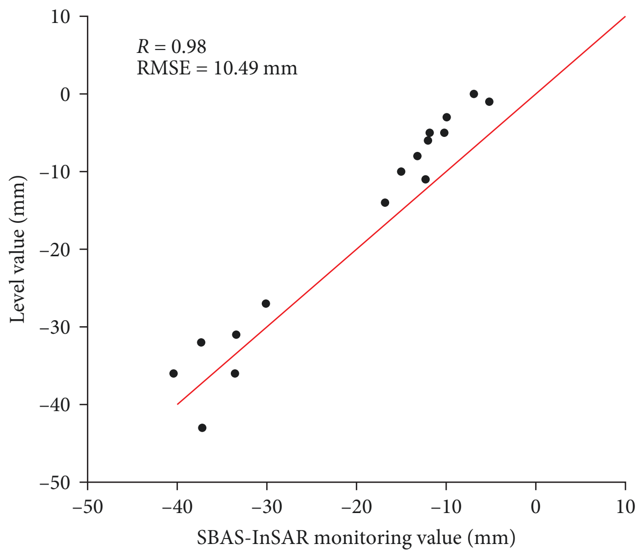

Figure 4: Comparison between the level measurement and SBAS monitoring results.

indicating that they are highly correlated with a linear correlation distribution. The RMSE is 10.486 mm.

Above all, the InSAR monitoring results of surface deformation are in good agreement with the level measurement data in the study area, and the overall change trend is consistent. It is proved that the SBAS-InSAR monitoring results of surface deformation are very reliable. Therefore, the use of the same data and SBAS-InSAR technology in Pan'an New City could obtain the same accuracy, which can meet the requirements of surface deformation monitoring in the mining subsidence area of Pan'an New City.

3. Results

3.1. Overview of the Study Area. Pan'anhu is located in Pan'anhu Street, Jiawang District, Xuzhou City, Jiangsu Province. It is an important part of the construction of Pan'an New City. The Quantai Coal Mine of Xuzhou Coal Mining Group is in the area. It is located in the middle of the main urban area of Xuzhou and the urban area of Jiawang, 18 km away from both places. Part of the mining-induced subsidence area of Quantai Coal Mine has been transformed into Pan'an Lake Wetland Park, and other subsidence lands have been included in the construction plan of Pan'an New City. In Mar. 2010, the coal mining subsidence area was officially transformed by Jiawang District. The total planned area is 52.89 km^2, including 16 km^2 in the core area. Phase I project was fully completed, with an investment of 1.4 billion yuan. The total area of the park is 11 km^2. The water area is 9.21 km^2. There are 160,000 trees, 1 million m^2 of flowers and vegetation, 980,000 m^2 of aquatic plants, more than 300 varieties, and 19 wetland islands. In June 2014, Pan'an Lake Wetland Park was rated as a national AAAA tourist attraction by the China National Tourism Administration.

In order to promote sustainable development of Pan'an Lake area, Pan'an New City, with a planned area of about 52.87 km^2 (including 7.5 km^2 of the completed area of Pan'an Lake Wetland Park), is planned to be built in this area since 2020, starting from 206 National Highway in the east, ending at Xuzhou branch of Beijing–Hangzhou Grand Canal in the south, the special railway line of the mining bureau in the west, Xujia Expressway in the north, and the fourth ring road. The core area is about 8 km^2, as shown in the green wireframe in Figure 5. The mined-out areas are shown in the red wireframe.

3.2. Data Preparation and Processing. Sentinel-1A data were used. Sentinel-1 consists of two polar orbiting satellites A and B, which are included in the active microwave remote sensing satellite whose sensors are carried in the C-band. The accuracy of surface deformation obtained from Sentinel-1A data can reach centimeter level, and even reach millimeter level in some areas with high coherence, such as cities, mining areas, etc. [34, 35]. Therefore, the surface deformation of Pan'an Lake in Xuzhou can be monitored with Sentinel-1A data to achieve the expected accuracy. In this paper, the adopted interferometric wide (IW) swath mode is the main acquisition mode over land. Two hundred fifty kilometers of data were collected, with a spatial resolution of 5 m × 20 m (single view). Compared with SM, EW, and WV, IW has a wider scanning range and is more suitable for monitoring land areas. Single look complex (SLC) can obtain phase and amplitude information [36]. Phase information is a function of time, and distance can be measured according to phase information and speed. SLC can be used for ranging and deformation observation [20].

The average unique rate, the temporal, and spatial baselines had nonlinear power function relationships with the coherence, respectively. The critical value of the length of the spatial vertical baseline of less than one-third of 2,000 m had a good coherence [10]. In this paper, the coherence result was sound in the image differential interferometric alignment. While the selection of the time baseline should fully consider the changes of ground layer and underground composition, seasons, climate, etc. Especially for areas with rich vegetation, images in winter should be used as far as possible for interference, so as to get better coherence effects. In the paper, the data of the spatiotemporal baseline for a whole year were selected. With the change of the four seasons, the coherence was directly affected and showed periodic changes, as shown in Figure 6.

3.2.1. Monitoring Results and Analysis. In this paper, the SBAS-InSAR technology was used to process 29 scene SAR data (Table 3). After the interferograms were cut, the interference pairs were screened, and the interference pairs with low coherence and poor interference effect were removed. Finally, they were applied to time series analysis. The data on 2021/06/28 were selected as the super main image and matched other images during interference processing. The high-resolution DEM was used to remove terrain phase, and get data images, unwrapping results, result maps, final results of data points, etc. After many experiments, the threshold value of the unwrapping coherence coefficient was finally set to 0.1, thus retaining most of the strongholds and control points, and obtaining the situations of all points and the

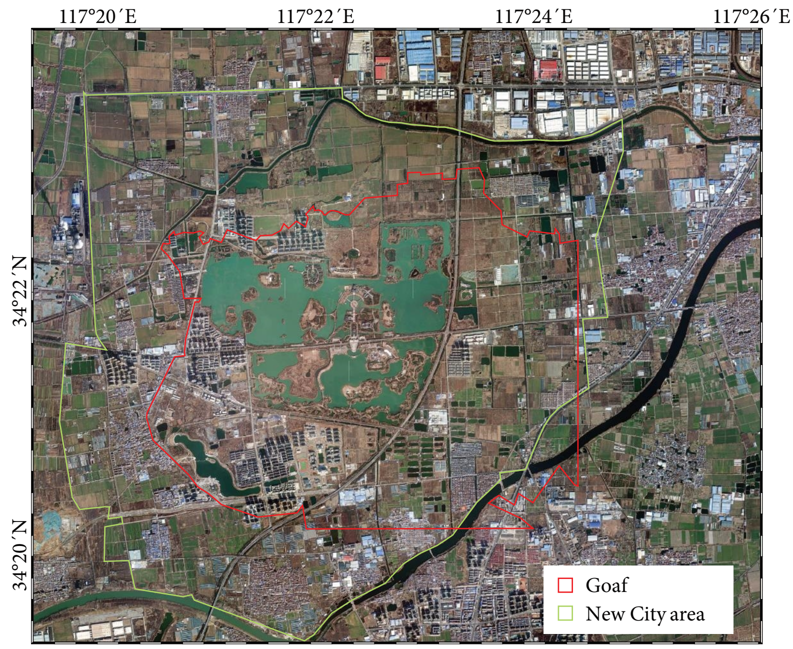

Figure 5: Image of Pan'an Lake.

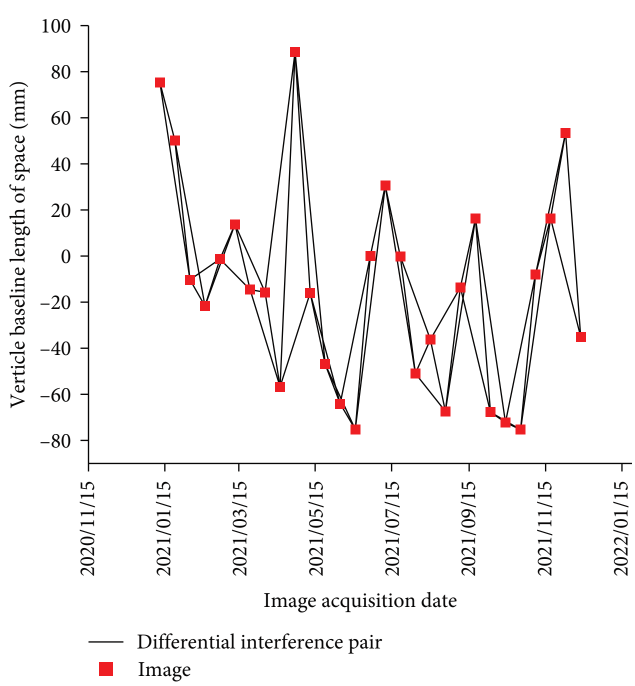

Figure 6: Spatiotemporal baselines.

surface deformation rate in deformation sites with centimeter accuracy in Pan'an Lake area.

The average displacement rate map and data loading of all points could be seen through the map matching the result points with optical images and superimposing GEO data. The unit of surface deformation is m/year. The ArcMap was used to overlay the optical base map of data points and get surface subsidence rates of Pan'an New City from Dec. 2020 to Jan. 2022. Figure 7 shows the final map.

It can be seen that there are two obvious uplifts in the west and northeast of Pan'an New City, obvious subsidence in the north, and no obvious uplift or subsidence in the south of the deformation area. Specifically:

(1) The average annual subsidence rate in the northern part could reach 40–163 mm/a.
(2) The subsidence rate could reach 13–83 mm/a and the uplift rate could reach 29–52 mm/a in Zhaozhuang and Shanghu areas in the northwest.
(3) The annual average rising rate of the relevant target points could reach 13–52 mm/a in the northeast and west.
(4) The uplift rate could reach −0.4–13 mm/a in the south.
(5) The uplift rate could reach 52–146 mm/a and the subsidence rate could reach 40–59 mm/a in Pan'an Lake area.

According to the evaluation criteria for the stability of goafs by longwall mining in the Code for Geotechnical Engineering Investigation of Coal Mine Goaf (Table 4), the accumulated surface subsidence is less than 60 mm in 12 months. Therefore, the goaf site in the north and northwest of Pan'an New City is unstable, while other areas are stable. It is necessary to strengthen monitoring and management during the construction of Pan'an New City on unstable sites to prevent accidents.

3.3. Discussion. In order to further analyze the surface deformation in the planning area of Pan'an New City from Dec. 2020 to Jan. 2022, five key research areas with obvious deformation were selected in the planning area, and nine points were randomly selected to analyze the temporal deformation of the surface, as shown in Figure 6.

3.3.1. Deformation Analysis and Planning Proposal for Area 1. Through processing the monitoring results, the surface deformation rate map of selected points was made in Area 1 from

Table 3: Sentinel-1A image data information in Pan'an Lake area.

No.	Satellite	Date	Orbit	No.	Satellite	Date	Orbit
1	Sentinel-1	2020/12/30	Ascending	17	Sentinel-1	2021/07/10	Ascending
2	Sentinel-1	2021/01/11	Ascending	18	Sentinel-1	2021/07/22	Ascending
3	Sentinel-1	2021/01/23	Ascending	19	Sentinel-1	2021/08/03	Ascending
4	Sentinel-1	2021/02/04	Ascending	20	Sentinel-1	2021/08/15	Ascending
5	Sentinel-1	2021/02/16	Ascending	21	Sentinel-1	2021/08/27	Ascending
6	Sentinel-1	2021/02/28	Ascending	22	Sentinel-1	2021/09/08	Ascending
7	Sentinel-1	2021/03/12	Ascending	23	Sentinel-1	2021/09/20	Ascending
8	Sentinel-1	2021/03/24	Ascending	24	Sentinel-1	2021/10/02	Ascending
9	Sentinel-1	2021/04/05	Ascending	25	Sentinel-1	2021/10/14	Ascending
10	Sentinel-1	2021/04/17	Ascending	26	Sentinel-1	2021/10/26	Ascending
11	Sentinel-1	2021/04/29	Ascending	27	Sentinel-1	2021/11/07	Ascending
12	Sentinel-1	2021/05/11	Ascending	28	Sentinel-1	2021/11/19	Ascending
13	Sentinel-1	2021/05/23	Ascending	29	Sentinel-1	2021/12/01	Ascending
14	Sentinel-1	2021/06/04	Ascending	30	Sentinel-1	2021/12/13	Ascending
15	Sentinel-1	2021/06/16	Ascending	31	Sentinel-1	2022/01/06	Ascending
16	Sentinel-1	2021/06/28	Ascending	—	—	—	—

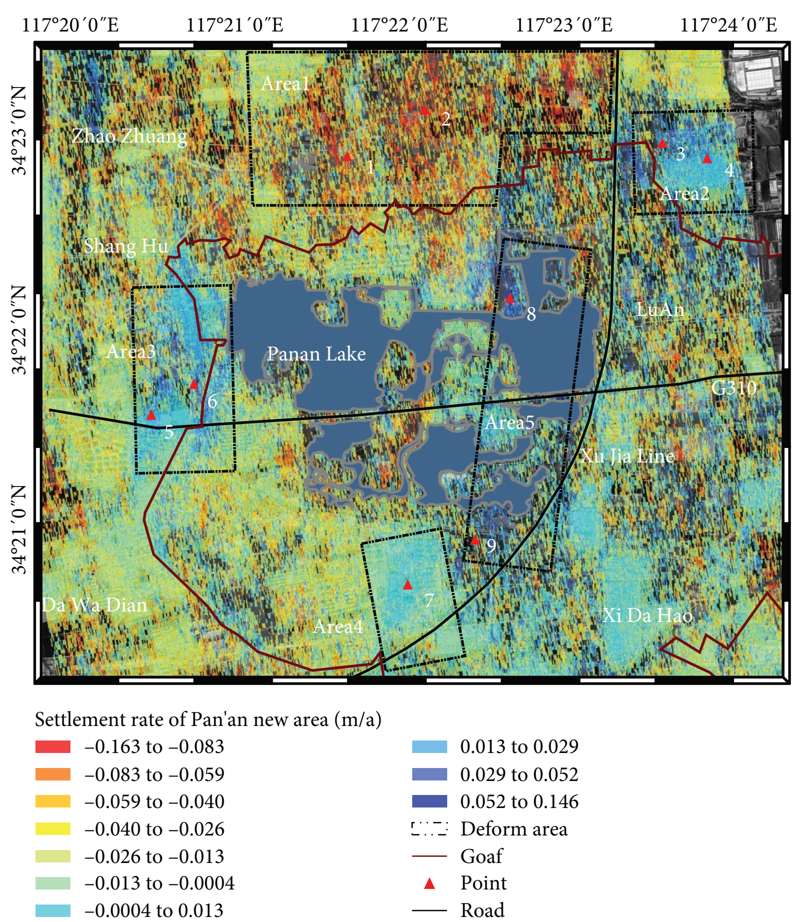

Figure 7: Surface subsidence rates of Pan'an New City from 2020/12/12 to 2022/01/01.

Dec. 2020 to Jan. 2022, as shown in Figure 8. It can be seen that the two points selected in Area 1 have smaller orders of magnitude of time series surface deformation, and the subsidence shows up and down fluctuations. The time series diagram of subsidence shows a fluctuation sinusoidal trend. The middle and right subsidence areas are mostly farmland and undeveloped commercial land. The left is composed of an ecological town and a part of farmland, where large-scale

Table 4: Evaluation criteria for site stability of goaf by longwall mining based on surface subsidence observation values.

Stability levels	Surface subsidence (mm)			
	1 month	3 months	6 months	12 months
Stable	≤5	≤15	≤30	≤60
Basically stable	5–10	15–30	30–60	60–120
Understable	10–30	30–60	60–120	120–240
Unstable	≥30	≥60	≥120	≥240

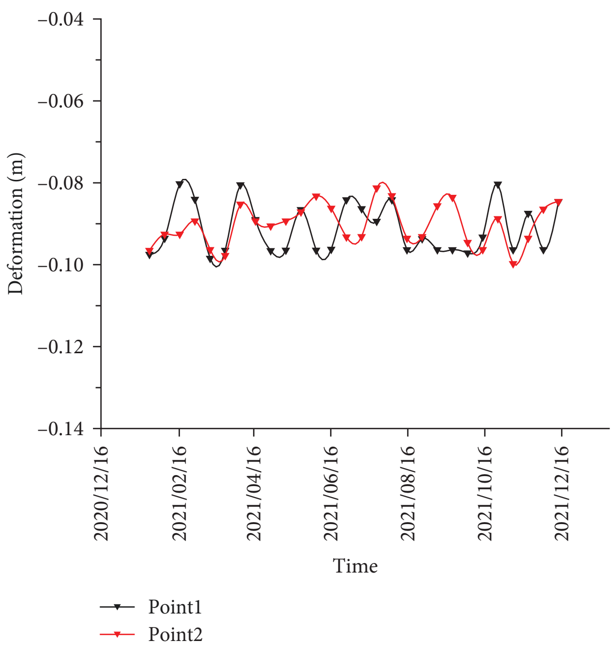

Figure 8: Deformation rates of selected points in Area 1 from Dec. 2020 to Jan. 2022.

subsidence occurs frequently. The average annual decline rate of the CT points in this area can reach 80–100 mm/a. According to the code, the goaf site is unstable in Area 1. According to the image analysis, the northern area of the proposed Pan'an New City is under large-area construction and development and compaction of the ground because of the construction of new skyscrapers before Dec. 2020, so the construction of the main works and ancillary works will further affect the stability of the goaf. If the construction of high-rise residential areas is planned, further assessment is required.

3.3.2. Deformation Analysis and Planning Proposal for Area 2. Figure 9 shows the deformation rate map in Area 2 consisting of farmland and a small part of greening. The selected two points are rising. The average annual rising rate of the relevant target points can reach 17–35 mm/a. According to Table 4, the goaf site is stable in Area 2.

After the construction in 2021, the surface deformation has gradually recovered to the normal uplift. The uplift deformation was obvious at the initial stage of the construction, and it became stable. Therefore, this area can be built into a shopping center, a prosperous business district, and a modern logistics comprehensive park. The area should strengthen cooperation with regional

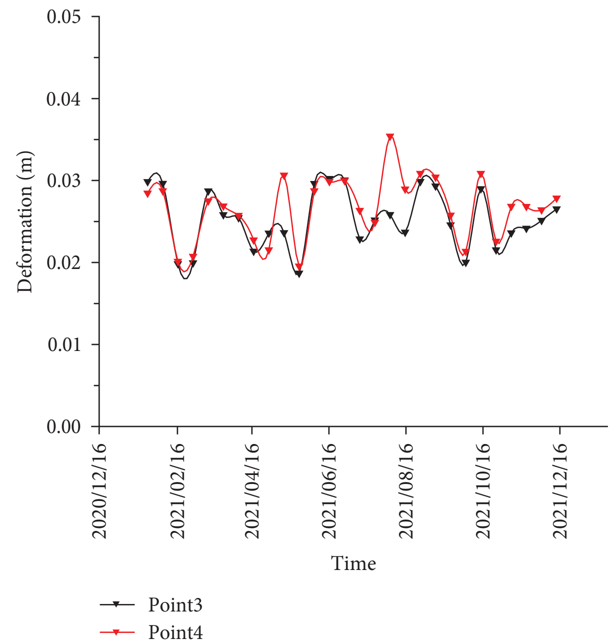

Figure 9: Deformation rates of selected points in Area 2 from Dec. 2020 to Jan. 2022.

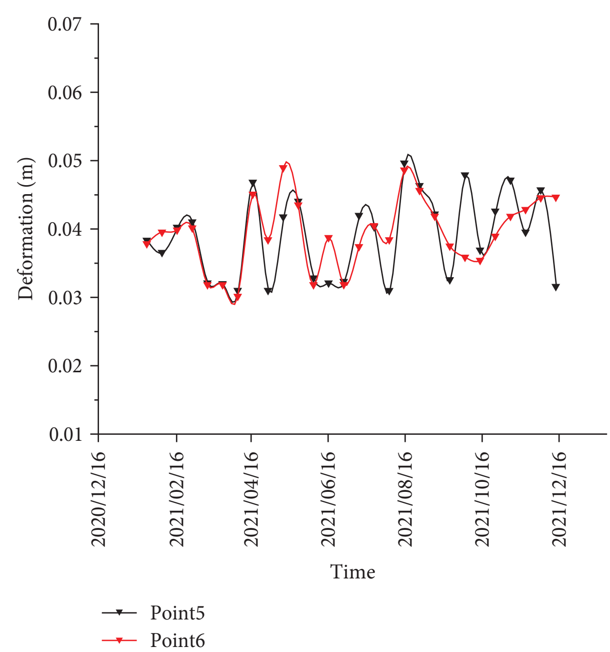

Figure 10: Deformation rates of selected points in Area 3 from Dec. 2020 to Jan. 2022.

leading industries and carry out effective transformation and upgrading of the service industry.

3.3.3. Deformation Analysis and Planning Proposal for Area 3. Figure 10 shows the surface deformation rates of points in Area 3. They show significant increases. The real estate is in Area 3, with basically high-rise buildings, some urban greening and some newly developed building areas. The average

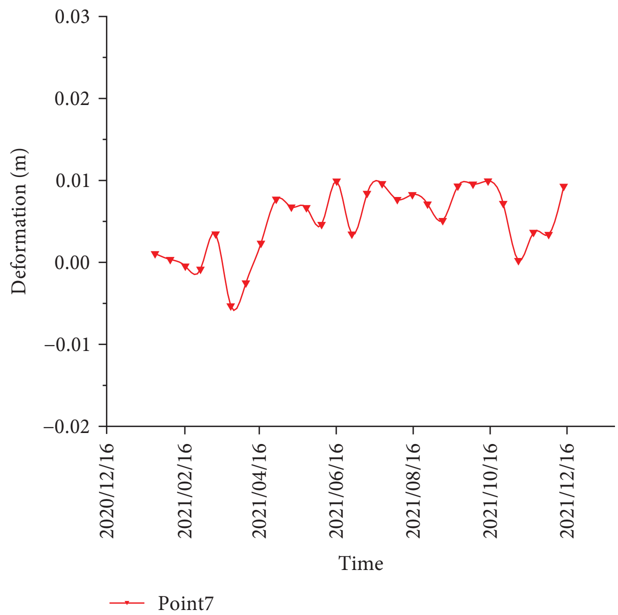

FIGURE 11: Deformation rates of selected points in Area 4 from Dec. 2020 to Jan. 2022.

annual rising rate of the CT points can reach 28–50 mm/a. According to Table 4, the goaf site is stable in Area 3.

The western region has been under frequent construction of real estate projects and the development of tourist areas in the Pan'an Lake area since 2021, so the time series deformation has a large fluctuation. As a potential resource around the Pan'an Lake Wetland Park, this area can be developed into a folk culture village. Combining its rural cultural characteristics, it can create an integrated industrial system of leisure and entertainment and develop service industries, such as homestays, etc. At the same time, starting from the agricultural supply-side structural reform, the region can vigorously develop characteristic crops, such as strawberries, cherries, and organic vegetables. Along with the construction of picking gardens, the region can build crop industrial parks, develop green brands of local vegetables, fruits and crops, improve the influence of local vegetables and fruits, and strive to achieve the integration of agricultural, industrial, and tourism industries. Quantai Coal Mine Museum is also one of the attractions, and the industrial sites can be preserved to create a diverse tourism experience.

3.3.4. Deformation Analysis and Planning Proposal for Area 4. Figure 11 shows the surface deformation rates of points in Area 4. The selected points in Area 4 show an upward trend. The area is composed of Pan'anhu Campus of School of Chinese Language and Literature of Jiangsu Normal University and some commercial buildings. The rising rate is −0.4 to 10 mm/a. The deformation was small, and the goaf site was stable.

There are a large number of industrial parks, residential areas, high-rise buildings, and roads in this area. It is also connected to the river. In order to ensure the well-being and stability of the Pan'an New City, the monitoring and management of this area should be strengthened constantly. The government can use the specific resource advantages of colleges and universities to provide scientific research bases for them, and use the disciplinary advantages to develop diversified industries such as building cultural industry parks.

3.3.5. Deformation Analysis and Planning Proposal for Area 5. Figure 12 shows the surface deformation rates of points in Area 5. The selected two points show different trends. Point8 showed an upward trend with fluctuations before June 2021, a downward trend from June 2021 to Oct. 2021, and a rising trend from Oct. 2021 to Jan. 2022. The uplift rate is 90–110 mm/a. Point9 shows a settlement trend, with a settlement rate of 40–55 mm/a. Considering the deformation area in Pan'an Lake, it will not affect the construction of Pan'an New City.

As the central area for the construction of Pan'an New City, Area 5 has completed the construction of Pan'an Lake Scenic Area, Pan'an Lake Wetland Park, Pan'an Water Town, Pan'an Lake Amusement Park, Pan'an Lake Cultural Park with the theme of loyalty and filial piety, forming a tourism integration. On this basis, the construction of the comprehensive transportation network system should be improved, and the supporting facilities should be optimized, such as public service facilities, etc.

4. Conclusions

In this paper, the accuracy of InSAR monitoring of coal mining subsidence was first verified. Then, SBAS-InSAR technology was used to monitor the surface subsidence in the proposed Pan'an New City area from Dec. 2020 to Jan. 2022. The monitoring results were analyzed comprehensively, and the stability of the goaf sites was evaluated. The main conclusions are as follows:

(1) With the working faces of a coal mine near Pan'an New City as the research objects, the measured leveling data and the SBAS-InSAR monitoring results of the mining-induced surface deformation were compared and analyzed. The RMSE was 10.49 mm, which proves the reliability of SBAS-InSAR technology for monitoring surface deformation in coal mining. Thus, SBAS-InSAR technology can be used to monitor surface deformation in the mining subsidence area of Pan'an New City.

(2) The average annual subsidence rates were 40–163mm and 13–83 mm/a in the north of Pan'an Lake, and Zhaozhuang and Shanghu areas in northwest of Pan'an New City, respectively. The average annual rising rate was 13–52 mm/a in Pan'an Village in the northeast and Mazhuang area in the west. The average annual rising rate was 0.4–13 mm/a in Pan'an Lake campus of Jiangsu Normal University and Xidawu Village in the south. The uplift rate could reach 52–146 mm/a and the subsidence rate can reach 40–90 mm/a in the Pan'an Lake area.

(3) According to the evaluation criteria for the stability of the goaf site by longwall mining in the Code for Geotechnical Engineering Investigation of Coal Mine Goafs, the goaf site in the north and northwest of

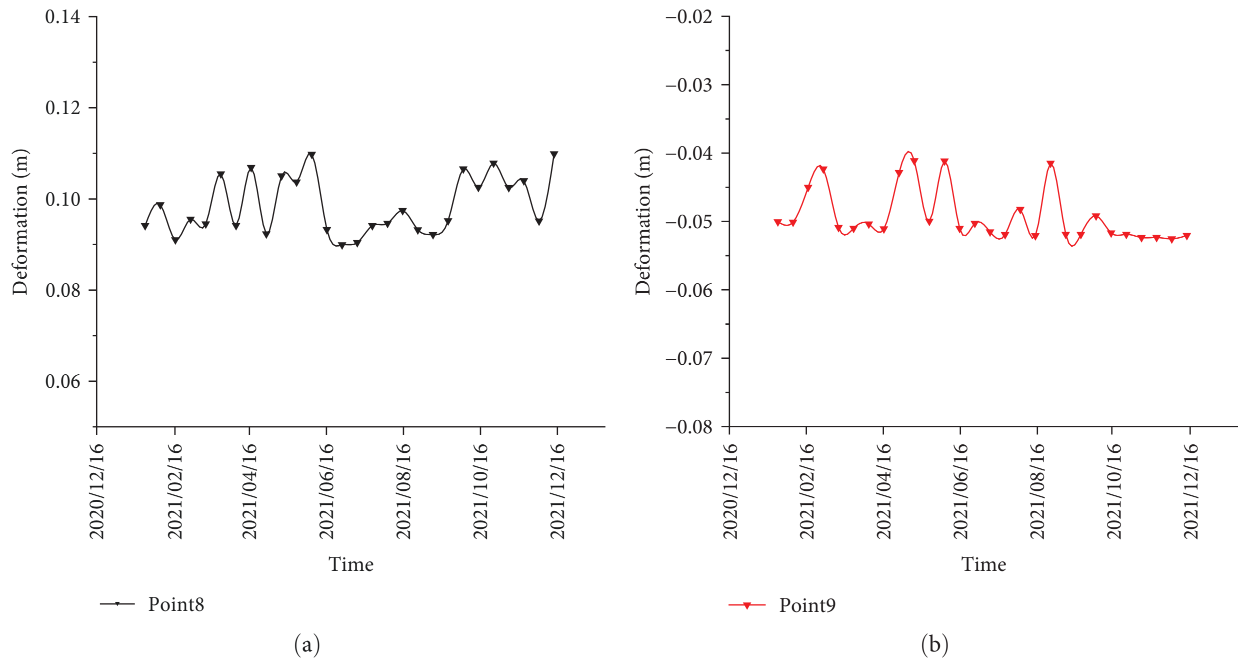

Figure 12: Deformation rates of selected points in Area 5 from Dec. 2020 to Jan. 2022: (a) description of Point8 in the Area 5 and (b) description of Point9 in the Area 5.

Pan'an New City is unstable, while other areas are stable. However, considering the influence of the construction of large buildings, such as high-rise buildings and elevated road buildings, the area of Pan'an New City shall be further evaluated and monitored during construction.

Data Availability

The data used to support the findings of this study are available from the corresponding author.

Conflicts of Interest

The authors declare that they have no conflicts of interest.

Acknowledgments

This research was funded by the Natural Science Foundation of Jiangsu Province (BK20220158), the Scientific Research Project of Jiangsu Bureau of Geological and Mineral Exploration (2021KY08), and the Postgraduate Research & Practice Innovation Program of Jiangsu Province (SJCX23_1316).

References

[1] Y. Q. Liu, *Study on Transformation Model and Comprehensive Benefit of Pan'an Lake Coal Mining Subsidence Area in Xuzhou*, China Mining University, Xuzhou, 2020.
[2] S. Qiu, Q. Yu, T. Niu et al., "Study on the landscape space of typical mining areas in Xuzhou city from 2000 to 2020 and optimization strategies for carbon sink enhancement," *Remote Sensing*, vol. 14, no. 17, Article ID 4185, 2022.
[3] X. Cui, Y. Zhao, G. Wang, B. Zhang, and C. Li, "Calculation of residual surface subsidence above abandoned longwall coal mining," *Sustainability*, vol. 12, no. 4, Article ID 1528, 2020.
[4] R. Bamler and P. Hartl, "Synthetic aperture radar interferometry," *Inverse Problems*, vol. 14, no. 4, pp. R1–R54, 1998.
[5] J. Pfeffer and P. Allemand, "The key role of vertical land motions in coastal sea level variations: a global synthesis of multisatellite altimetry, tide gauge data and GPS measurements," *Earth and Planetary Science Letters*, vol. 439, pp. 39–47, 2016.
[6] M. Komac, R. Holley, P. Mahapatra, H. van der Marel, and M. Bavec, "Coupling of GPS/GNSS and radar interferometric data for a 3D surface displacement monitoring of landslides," *Landslides*, vol. 12, no. 2, pp. 241–257, 2015.
[7] B. Hu, L. Chen, Y. Zou, X. Wu, and P. Washaya, "Methods for monitoring fast and large gradient subsidence in coal mining areas using SAR images: a review," *IEEE Access*, vol. 9, pp. 159018–159035, 2021.
[8] T. Peternel, Š. Kumelj, K. Oštir, and M. Komac, "Monitoring the Potoška planina landslide (NW Slovenia) using UAV photogrammetry and tachymetric measurements," *Landslides*, vol. 14, no. 1, pp. 395–406, 2017.
[9] H. Rott, "Advances in interferometric synthetic aperture radar (InSAR) in earth system science," *Progress in Physical Geography: Earth and Environment*, vol. 33, no. 6, pp. 769–791, 2009.
[10] Z. Yang, Z. Li, J. Zhu, Y. Wang, and L. Wu, "Use of SAR/InSAR in mining deformation monitoring, parameter inversion, and forward predictions," *IEEE Geoscience and Remote Sensing Magazine*, vol. 8, no. 1, pp. 71–90, 2020.
[11] Y. Zhang, Y. Liu, M. Jin et al., "Monitoring land subsidence in Wuhan city (China) using the SBAS-InSAR method with radarsat-2 imagery data," *Sensors*, vol. 19, no. 3, Article ID 743, 2019.
[12] M. Xiexing and Q. Minggao, "Research status and prospect of green mining of coal resources in China," *Journal of Mining & Safety Engineering*, vol. 26, no. 1, pp. 1–14, 2009.
[13] Y. Dong, L. Zhang, and M. Liao, "Improved topographic mapping in vegetated mountainous areas by high-resolution

radar-grammetry-assisted sar interferometry," *ISPRS Annals of the Photogrammetry, Remote Sensing and Spatial Information Sciences*, vol. V-3-2020, pp. 133–139, 2020.

[14] Y. Xu, T. Li, X. Tang, X. Zhang, H. Fan, and Y. Wang, "Research on the applicability of DInSAR, stacking-InSAR and SBAS-InSAR for mining region subsidence detection in the Datong coalfield," *Remote Sensing*, vol. 14, no. 14, Article ID 3314, 2022.

[15] A. Hooper, D. Bekaert, K. Spaans, and M. Arikan, "Recent advances in SAR interferometry time series analysis for measuring crustal deformation," *Tectonophysics*, vol. 514–517, pp. 1–13, 2012.

[16] R. Goldstein, "Atmospheric limitations to repeat-track radar interferometry," *Geophysical Research Letters*, vol. 22, no. 18, pp. 2517–2520, 1995.

[17] A. Hooper, P. Segall, and H. Zebker, "Persistent scatterer interferometric synthetic aperture radar for crustal deformation analysis, with application to Volcán Alcedo, Galápagos," *Journal of Geophysical Research: Solid Earth*, vol. 112, no. B7, Article ID B7407, 2007.

[18] P. Berardino, G. Fornaro, R. Lanari, and E. Sansosti, "A new algorithm for surface deformation monitoring based on small baseline differential SAR interferograms," *IEEE Transactions on Geoscience and Remote Sensing*, vol. 40, no. 11, pp. 2375–2383, 2002.

[19] B. Osmanoğlu, F. Sunar, S. Wdowinski, and E. Cabral-Cano, "Time series analysis of InSAR data: methods and trends," *ISPRS Journal of Photogrammetry and Remote Sensing*, vol. 115, pp. 90–102, 2016.

[20] Y. Chen, S. Yu, Q. Tao, G. Liu, L. Wang, and F. Wang, "Accuracy verification and correction of D-InSAR and SBAS-InSAR in monitoring mining surface subsidence," *Remote Sensing*, vol. 13, no. 21, Article ID 4365, 2021.

[21] Z. Yang, Z. Li, J. Zhu et al., "Locating and defining underground goaf caused by coal mining from space-borne SAR interferometry," *ISPRS Journal of Photogrammetry and Remote Sensing*, vol. 135, pp. 112–126, 2018.

[22] B. Chen, H. Yu, X. Zhang et al., "Time-varying surface deformation retrieval and prediction in closed mines through integration of SBAS InSAR measurements and LSTM algorithm," *Remote Sensing*, vol. 14, no. 3, Article ID 788, 2022.

[23] J. Baek, S.-W. Kim, H.-J. Park, H.-S. Jung, K.-D. Kim, and J. W. Kim, "Analysis of ground subsidence in coal mining area using SAR interferometry," *Geosciences Journal*, vol. 12, no. 3, pp. 277–284, 2008.

[24] G. Cianflone, C. Tolomei, C. Brunori, and R. Dominici, "InSAR time series analysis of natural and anthropogenic coastal plain subsidence: the case of Sibari (Southern Italy)," *Remote Sensing*, vol. 7, no. 12, pp. 16004–16023, 2015.

[25] Y. Han, J. Zou, Z. Lu, F. Qu, Y. Kang, and J. Li, "Ground deformation of Wuhan, China, revealed by multi-temporal InSAR analysis," *Remote Sensing*, vol. 12, no. 22, Article ID 3788, 2020.

[26] V. Akbari and M. Motagh, "Improved ground subsidence monitoring using small baseline sar interferograms and a weighted least squares inversion algorithm," *IEEE Geoscience and Remote Sensing Letters*, vol. 9, no. 3, pp. 437–441, 2012.

[27] J. Liu, J. Hu, Z. Li et al., "Complete three-dimensional coseismic displacements due to the 2021 Maduo earthquake in Qinghai province, China from Sentinel-1 and ALOS-2 SAR images," *Science China Earth Sciences*, vol. 65, no. 4, pp. 687–697, 2022.

[28] S. Haji-Aghajany and Y. Amerian, "Assessment of InSAR tropospheric signal correction methods," *Journal of Applied Remote Sensing*, vol. 14, no. 4, Article ID 14, 2020.

[29] W. Gong, D. Zhao, C. Zhu et al., "A new method for InSAR stratified tropospheric delay correction facilitating refinement of coseismic displacement fields of small-to-moderate earthquakes," *Remote Sensing*, vol. 14, no. 6, Article ID 1425, 2022.

[30] P. K. Kirui, E. Reinosch, N. Isya, B. Riedel, and M. Gerke, "Mitigation of atmospheric artefacts in multi temporal InSAR: a review," *PFG—Journal of Photogrammetry, Remote Sensing and Geoinformation Science*, vol. 89, no. 3, pp. 251–272, 2021.

[31] S. Haji-Aghajany and Y. Amerian, "Atmospheric phase screen estimation for land subsidence evaluation by InSAR time series analysis in Kurdistan, Iran," *Journal of Atmospheric and Solar-Terrestrial Physics*, vol. 205, Article ID 105314, 2020.

[32] K. Biswas, D. Chakravarty, P. Mitra, and A. Misra, "Spatial-correlation based persistent scatterer interferometric study for ground deformation," *Journal of the Indian Society of Remote Sensing*, vol. 45, no. 6, pp. 913–926, 2017.

[33] Q. Chen, G. Liu, J. Hu, X. Ding, and Y. Yang, "Mapping ground 3-D displacement with GPS and PS-InSAR networking in the Pingtung area, southwestern Taiwan, China," *Chinese Journal of Geophysics*, vol. 55, no. 10, pp. 3248–3258, 2012.

[34] E. Chaussard, F. Amelung, H. Abidin, and S.-H. Hong, "Sinking cities in Indonesia: ALOS PALSAR detects rapid subsidence due to groundwater and gas extraction," *Remote Sensing of Environment*, vol. 128, pp. 150–161, 2013.

[35] F. Lin, L. Deng, and X. U. Zhijie, "Application of InSAR technology in surface deformation monitoring in mining area," *Energy and Environmental Protection*, vol. 44, no. 2, pp. 182–185, 2022.

[36] C. Werner, U. Wegmüller, T. Strozzi, and A. Wiesmann, "Gamma SAR and interferometric processing software," in *Proceedings of the ERS-ENVISAT Symposium*, pp. 16–20, 2000.